https://doi.org/10.1016/j.dyepig.2020.108209

Highly photostable ketopyrrolyl-BODIPYs with red aggregation-induced emission characteristics for ultrafast wash-free mitochondria-targeted bioimaging

Hao Wu,[†] Xing Guo,[†] Changjiang Yu,*[,†,‡,§] Wai-Yeung Wong,[‡] Erhong Hao[†] and Lijuan Jiao*[,†]

[†]*The Key Laboratory of Functional Molecular Solids, Ministry of Education, Anhui Laboratory of Molecule-Based Materials, School of Chemistry and Materials Science, Anhui Normal University, Wuhu 241000, China.* E-mail: jiao421@ahnu.edu.cn, yuchj@ahnu.edu.cn

[‡]*Department of Applied Biology and Chemical Technology, The Hong Kong Polytechnic University, Hung Hom, Kowloon, Hong Kong, China.*

[§]*State Key Laboratory of Coordination Chemistry, Nanjing University, Nanjing 210093, China.*

ABSTRACT: Subcellular organelle-specific probes, including mitochondria-targeted fluorescent probes, have attracted enormous research interests because they can monitor or visualize the morphology or biological activities of specific organelles and play an indispensable role in disease diagnosis. To follow the process, highly specific and photostable fluorescent probes are in demand. However, commercially available mitochondria probes normally suffer from poor photostability under laser irradiation and aggregation caused quenching (ACQ) in the aggregate state. In this work, two simple aggregation-induced emission(AIE)-active *meso*-2-ketopyrrolyl BODIPYs were developed *via* a convenient one-pot synthetic procedure from 2-methylpyrrole and corresponding pyrrolyldiketone in the presence of $BF_3 \cdot OEt_2$. The two AIE luminogens (AIEgens) both show very weak fluorescence (maximum emission peaks at 545 and 559 nm, respectively) in DMSO and strong near-infrared solid-state emission. The fluorescence was dramatically intensified and redshifted to 635 and 643 nm, respectively, when water fraction was increased up to above 95% in the DMSO/water mixtures. Both AIEgens were found to specifically "light up" the cell mitochondria with high biocompatibility. Interestingly, the staining process can be shortened for less than a minute after the addition of the AIEgens and without the involvement of a washing procedure, indicating an ultrafast and easy-to-operate staining protocol. Furthermore, their fluorescent images in deep tissue penetration were captured with a satisfied signal-to-noise ratio at a depth of 20 and 30 μm along the direction of the z-axis. Importantly, both AIEgens exhibit high photostability under harsh continuous laser irradiation, demonstrating their potential application as in visualizing and tracking specific mitochondria-associated dynamic changes.

KEYWORDS: BODIPY, aggregation-induced emission, fluorescent probes, high photostability, bioimaging

INTRODUCTION

Mitochondria, known as a powerhouse of almost all eukaryotic cells, are vital subcellular organelles and supply energy for various life activities. [1] For example, mitochondria can produce adenosine triphosphate (ATP), which involves a series of electron-transport processes and relates to the generation of reactive oxygen species (ROS).[1a,2] Mitochondria dysfunctions will lead to abnormal levels of ROS and eventually cause many diseases, such as human cardiovascular disease, neurodegenerative illnesses, Reye's syndrome, or tumors.[3]

Fluorescent bioimaging, as a non-invasive method for visualizing the processes of biological systems, holds great promise for early image-guided diagnosis due to its real-time monitoring with high resolution, high contrast, and high sensitivity.[4,5] Mitochondria-specific fluorescent probes that can selectively illuminate cellular mitochondria, can monitor or visualize their morphology or biological activities for studying apoptosis and degenerative conditions and thus play an indispensable role in disease diagnosis. To observe the long-term dynamic tracking in live samples, photostability is a particularly important parameter for fluorescence imaging.[6] However, traditional fluorescent probes especially commercial available mitochondria-specific dyes, such as MitoTracker® Green FM and MitoTracker® Deep Red FM, suffer from poor photo-stabilities under continuous laser irradiation. In addition, these commercially available probes show much weaker fluorescence when increasing their concentrations own to the aggregation-caused quenching (ACQ) effect.[7] The fluorescence quenching results from the formation of exciplex or excimers assisted by the intermolecular π-π stacking and/or dipole-dipole interactions of these fluorophores.[7,8] Thus, the luminescent intensities under continuous irradiation cannot be improved by increasing fluorophore concentration due to the accompanying ACQ effect.

Recently, organic aggregation-induced emission luminogens (AIEgens) with high luminescent efficiency have become a highly promising strategy to mitigate the ACQ effect.[9-12] Since the AIE phenomenon was found by Tang's group,[9] a variety of AIEgens have been developed, not only including designed fluorophores with novel structures but also classical fluorophores such as pyrene, coumarins, squaraines, perleneimides, cyanies, and boron dipyrromethenes (BODIPYs).[11,13,14] Various subcellular organelle-specific AIE probes were also developed for bioimaging. For example, Tang and coworkers developed a series of tetraphenylethene-derived AIEgens linked with mitochondria targeting triphenylphosphonium moieties and successfully applied mitochondrial imaging with high specificity and photostability for real-time monitoring, despite of their relatively short-wavelength emission.[6,15-18]

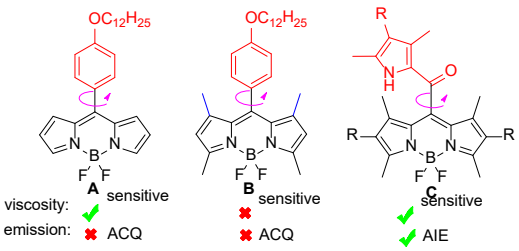

Fig. 1. The conventional *meso*-phenyl substituted BODIPY **A**, and BODIPYs **B** and **C** containing substituents on the 1,7-positions.

BODIPY dyes (Fig. 1), as an increasingly valuable class of fluorophores, have attracted much attention with their remarkable

achievements owing to their facile synthesis, easy modifications, and unique photophysical properties, including robust photo- and chemical-stability, high quantum yields, and large molar extinction coefficients.[19-23] They have been widely used for a wide array of different fields, such as fluorescence labeling, sensors, photosensitizers and so on.[23f,24] Unfortunately, similar to other traditional dyes, most of the BODIPY dyes also suffer from the ACQ effect and exhibit weak fluorescence in the aggregation state. To overcome the defects, limited BODIPY AIEgens have been recently developed *via J*-type aggregation[25], or through conjugation of BODIPY with known AIEgens[26] such as tetraphenylethene.

It has been found that various *meso*-arylBODIPYs **A** (Fig. 1) with no substituents on the 1,7-positions have been developed as efficient fluorescent molecular rotors based on the rotation of *meso*-phenyl group around a C-C single bond.[27] Increasing of viscosity makes it difficult for the *meso*-phenyl group to rotate and brings the increase in the fluorescence intensity. We noticed that restriction of intramolecular rotation (RIR) has been known as a main mechanism of AIE phenomenon.[28] However, attempts to study the emission of aggregated BODIPY **A** in binary THF and water solvent system gave an ACQ effect, despite of RIM of *meso*-phenyl group.[29] Similar ACQ effect was found for BODIPY **B**. The intermolecular π-π stackings of BODIPYs **A** and **B** are respossible for the ACQ effect.[14] Recently, we have developed *meso*-2-ketopyrrolyl-derived BODIPY **C** as fluorescent viscosimeter for real-time quantitative determination of intracellular viscosity variation in live cells.[30a] Interesting, in contrast to BODIPYs **A** and **B**, we found BODIPY **C** also showed interesting AIE phenomenon when increasing its concentration, which is promising for fluorescent bioimaging. Herein, we designed two novel *meso*-2-ketopyrrolyl BODIPY AIEgens and systematically studied their fluorescent bioimaging application. We found that both BODIPY AIEgens show deep red to near infrared emission upon aggregation and are able to specifically "light up" the cell mitochondria with high biocompatibility. Interestingly, both AIEgens could stain live cells through an ultrafast and easy-to-operate staining protocol. More importantly, both AIEgens exhibit high photostability under a harsh continuous laser irradiation, demonstrating their potential application in biomedical and materials science.

RESULTS AND DISCUSSION

Synthesis and characterization

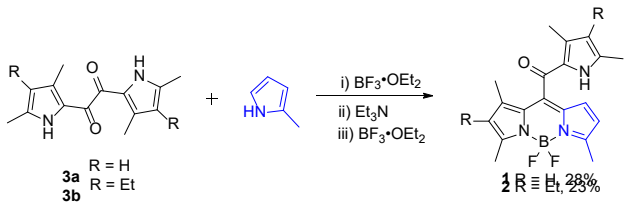

Scheme 1. Synthesis of probes **1** and **2**.

As shown in Scheme 1, BODIPYs **1** and **2** were synthesized simply via a one-pot reaction in 28% and 23% yields, respectively, by condensing 2-methylpyrrole with pyrrolyldiketone **3a** or **3b** promoted by $BF_3 \cdot OEt_2$, followed by in situ complexation with $BF_3 \cdot OEt_2$ in the presence of triethylamine. Pyrrolyldiketones **3a** and **3b** were synthesized from oxalyl chloride and 2,4-dimethylpyrrole or 2,4-dimethyl-3-ethylpyrrole according to previous work.[30a] Both **1** and **2** were well characterized by ^1H and ^{13}C NMR spectroscopy

as well as high resolution mass spectrometry. The structure of BODIPY **2** was further confirmed by X-ray single crystal structure analysis (Fig. 2).

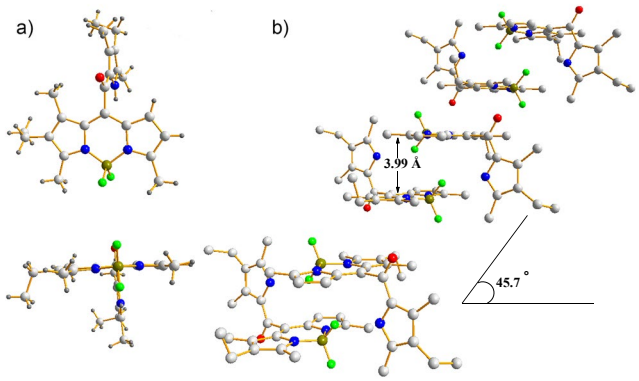

Fig. 2. (a) Front and side views of X-ray crystal structures for probe **2**. C, light gray; H, gray; N, blue; F, bright green; B, dark yellow; O, red. (b) Crystal-packing pattern of probe **2** between the adjacent interlayered crystals from side view. Interlayer distance is 3.99 Å and tilt angle is 45.7° for coplanar inclined arrangements of its transition dipole. H atoms are omitted for clarity.

Similar with the reported BF_2 complexes[19,20], the dipyrrin mean plane of **2** is almost planar (Fig. 2) although slightly distorted conformations were observed with a dihedral angle of 3.0° defined by two coordinated pyrrolic rings (Table S1). The crystallographic data were summarized in Tables S1 and S2 (SI). The average B-N distances (1.528 and 1.548 Å) are different, supporting its unsymmetrical structure. The carbonyl group and the uncoordinated pyrrole ring are coplanar in their crystals but the oxygen atom of the carbonyl group and the uncoordinated pyrrolic nitrogen are aligned in opposite direction. The dihedral angle between the *meso*-2-ketopyrrolyl core and the BODIPY core is almost vertical with 87.3(2)°. The twisted conformation of the ketopyrrolyl segment rigidified the intermolecular distance (3.99 Å) between two parallel BODIPY planes of the dimer with well-ordered head to head packings (Fig. 2). Besides, **2** adopts a slip angle of 45.7° for coplanar inclined arrangement, which is characteristic of *J*-type packing arrangements in accord with Kasha's rule.[25a]. This packing might prevent emission quenching in its aggregation state, which provides a solid foundation for its AIE characteristics studied later.

Photophysical properties

The normalized absorption and fluorescence spectra of **1** and **2** are shown in Figs. 3a, 3e and S4-S8, respectively, and the data are summarized in Tables 1 and S3 (SI). For example, **1** and **2** have absorption maxima at 514 and 524 nm in dimethyl sulfoxide (DMSO), with extinction coefficients of 4.57×10^4 and 5.50×10^4 $M^{-1}cm^{-1}$ and emission maxima at 545 and 559 nm (Table S3), respectively. Similar absorption and emission shapes are observed in other solvents. Despite few variations of the absorbance and fluorescence emission maxima were observed for them in different solvents, however, decreased absolute fluorescence quantum yields were obtained in more polar solvents (Table S3, Fig. S4-S7). For example, the fluorescence quantum yield of probe **1** is only 0.8% in DMSO, while this value increases to 12% in cyclohexane. Similarly, probe **2** also showed very weak fluorescence (emission maximum peak at 559 nm) with a fluorescence quantum yield of 0.2% in DMSO. In sharp contrast with those in polar solvents, both compounds show strong red fluorescence emission in their solid powder states with high fluorescence quantum yields of 0.30 and 0.29 (Table S3), respectively. In addition, their solid state emission bands are redshifted to near infrared region with emission

maxima at 699 and 711 nm for **1** and **2** (Figs. 3a and 3e), respectively, and these red fluorescence in solid state can be observed by naked eye under 365 nm UV lamp irradiation.

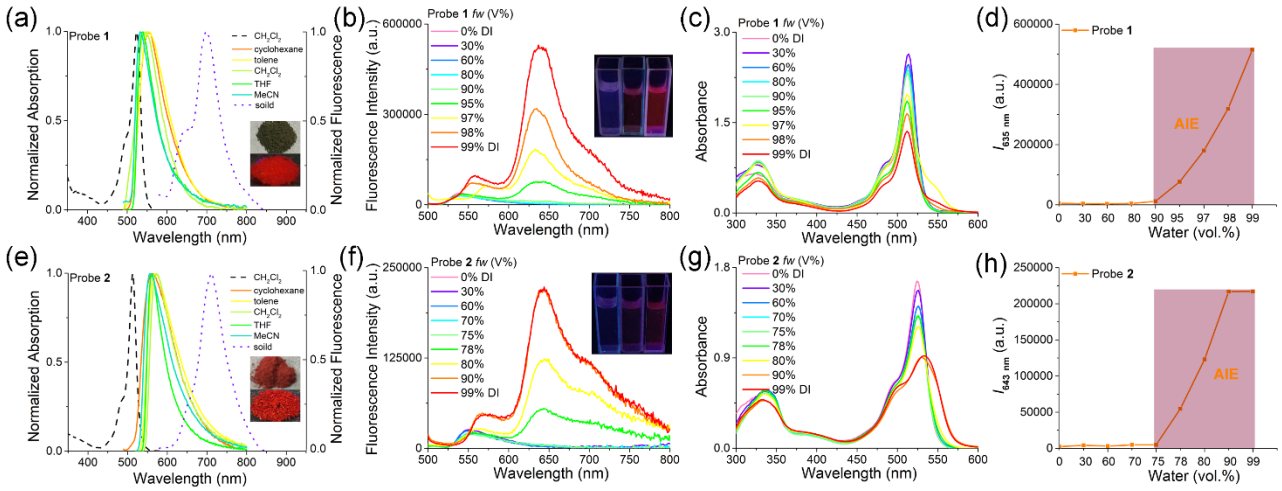

Fig. 3. (a), (e) Normalized absorption spectra (dotted black line, in cyclohexane solution), normalized fluorescence spectra (continuous line, in different solvents) and fluorescence emission in solid state spectra (purple dotted line) of probes **1** or **2**. Inserted photographs of their powders under daylight and 365 nm UV lamp irradiation. (b), (f) Fluorescence spectra of probes **1** or **2** (30 μM) in DMSO/ deionized water (DI) with different water fractions (*f*w), excited at 490 nm. Inserted photographs of probes **1** or **2** (30 μM), respectively in DMSO, and DMSO/DI system (95% and 99% water content) under 365 nm UV lamp irradiation. (c), (g) Absorption spectra of probes **1** or **2** (30 μM) in DMSO/DI with different water fractions (*f*w). (d), (h) Plot of the fluorescent intensity at 635 nm or 643 nm versus different water fractions (λ_{ex} = 490 nm).

Table 1. Photophysical properties of probes **1** and **2** in dimethyl sulfoxide and deionized water at room temperature.

dyes	solvents	λ_{abs}^{max} (nm)	λ_{em}^{max} (nm)	logε_{max} [a]	ϕ [b]	Stokes Shift (cm^{-1})
1	dimethyl sulfoxide	514	545	4.87	0.01	1107
	deionized water[c]	512	635	4.66	0.14	3783
2	dimethyl sulfoxide	524	550	4.74	0.002	902
	deionized water[c]	534	643	4.49	0.11	3175

[a] Molar absorption coefficient are in the maximum of the highest peak. [b] Fluorescence quantum yields of probes **1** and **2** were measured in dimethyl sulfoxide and deionized water by Edinburgh instrument FLS 1000 using integrating sphere. [c] Deionized water contains 1% DMSO.

Encouraged by their high solid fluorescence, we turned to study the AIE properties of BODIPYs **1** and **2** using DMSO and water as solvents to control the dissolution and aggregation of these fluorescent molecules. As shown in Fig. 3b, during the process of increasing the volume fraction of water from 0% to 90%, the fluorescence emission of **1** was weak and did not show obvious changes. However, when the water fraction further increased to reach 95%, the fluorescence intensity increases instantaneously with a new red-shifted emission peak with maximum at 635 nm, indicating **1** as an AIEgen. Similar AIE process with red-shifted emission peak with maximum at 643 nm was observed for BODIPY **2** (Fig. 3e). Especially after the water fraction increased to 99%, both dyes showed intense fluorescence with fluorescence quantum yields of 14% and 11% for **1** and **2**, respectively (Figs. 3d and 3h). With increasing the water fraction, both dyes showed slightly bathochromically shifted and broadened absorption spectra (Figs. 3c and 3g), indicating a possible formation of *J*-aggregates.

Mechanism of AIE and nanoparticle characterization.

In order to understand the mechanism of this AIE phenomenon, the absorption and emission spectra of both probes were investigated in different proportions of methanol and glycerol. It was observed that the fluorescence emission intensity of both **1** and **2** increases with the viscosity of the solution increasing, and there is a linear relationship between the luminescence intensity and the viscosity (Fig. 4). In contrast, only slightly redshifted absorption maxima for both probes were observed (Figs. 4a and 4e) with increasing the viscosity of the solution. These results indicate that, similar with that of BODIPY **A**, rotation of *meso*-2-ketopyrrolyl moiety in BODIPYs **1** and **2** is the main mechanism for their weak emission in organic solvents. However, in contrast to **A** which shows ACQ effect in aggregations, BODIPYs **1** and **2** exhibit AIE due to restriction of intramolecular rotation of *meso*-2-ketopyrrolyl moiety and formation of *J*-aggregates in aqueous solution.

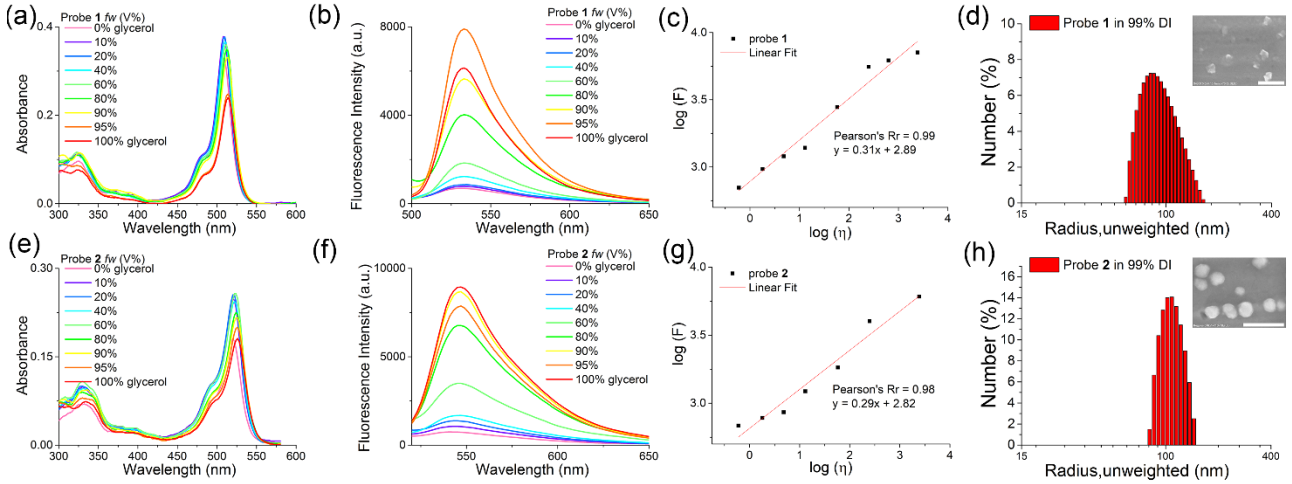

Fig. 4. (a), (e) Viscosity change of the absorbance spectra of probes **1** or **2** (5 μM) in methanol/glycerol mixtures. (b), (f) Viscosity change of the fluorescence emission spectra of probes **1** or **2** (5 μM) in methanol/glycerol mixtures, excited at 480 nm. (c), (g) Plot of the integral area of fluorescence intensity after the logarithm versus logarithm of viscosity value (log η). (d), (h) Dynamic light scattering data of probe **1** or **2** in the DMSO/DI system containing a deionized water fraction equal to 99%. The insets show SEM images, respectively for probes **1** and **2** NPs in the DMSO/DI system containing a deionized water fraction equal to 99%. Scale bar: 500 nm.

To further understand their aggregation behaviors, both **1** and **2** with a water fraction of 99% in the DMSO/DI system were subjected to scanning electron microscopy (SEM) study. It is interesting to observe that morphological structures of their nanoparticles (NPs) were obviously different. Probe **1** NPs exhibited a nano cuboid structure while probe **2** NPs showed a nanoball structure (Figs. 4d and 4h). The corresponding dynamic light scattering (DLS) measurements (Figs. 4d and 4h) revealed their average diameter sizes of 50 and 170 nm, respectively, for NPs of **1** and **2**, which are in good agreement with the sizes from SEM studies.

Cytotoxicity.

Before the application for cell imaging, the cytotoxicity of probes **1** and **2** was evaluated in Hela cells. Cells were exposed to the increasing amount of each probe for 24 h, and cell viability was detected by CCK-8 assay (Fig. 5). Both probes showed little cytotoxicity at the concentration up to 30 μM after being incubated for 24 h. Further cytotoxicity study of both probes at much

higher concentrations (up to 200 μM) after being incubated for 4 h was also evaluated (Fig. S25). The cell viabilities of both probes were basically over 80% at the concentration of 100 μM. These results indicated that probes **1** and **2** exhibited negligible cytotoxicity within the concentration ranges that were enough to evaluate their potential bioimaging application. Nevertheless, further fabrication methodology using biocompatible polymers without addition of DMSO solvent can be used, which may further decrease the cytotoxicity and increase the biocompatibility of the resultant nanoparticles.[31a]

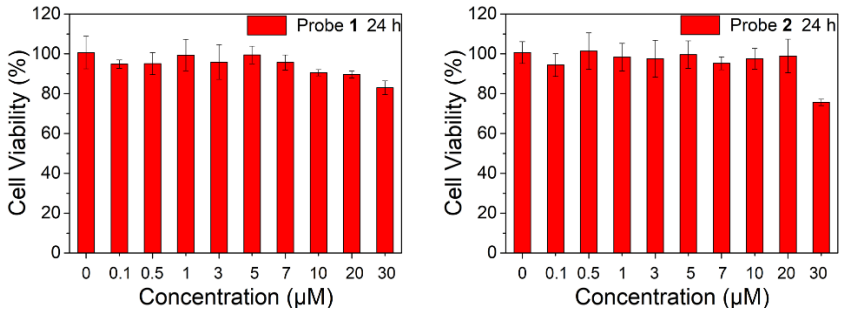

Fig. 5. Cytotoxicity of HeLa cells treated with different concentrations of probes **1** (left) and **2** (right) for 24 h as demonstrated by CCK-8 assay.

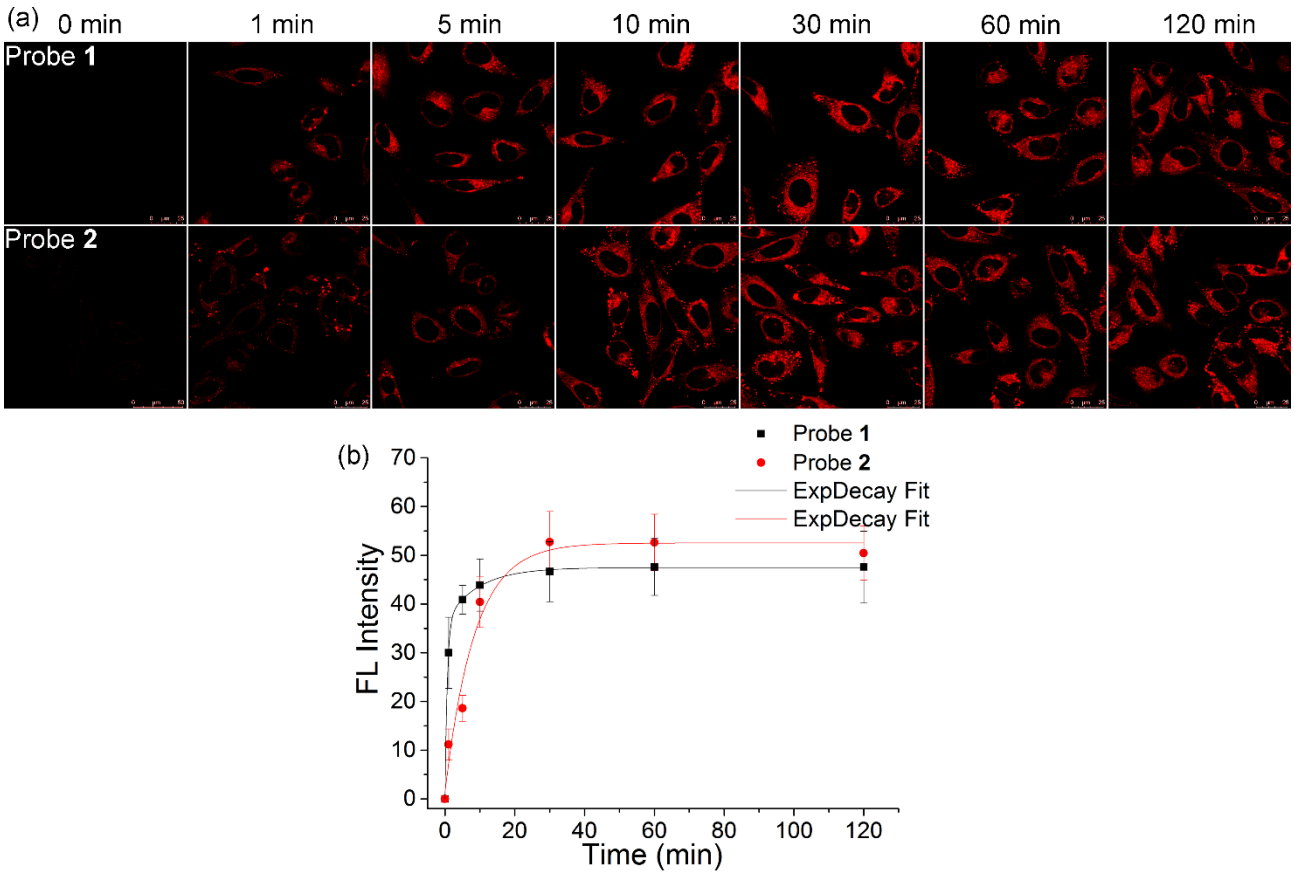

Fig. 6. (a) CLSM images of time-dependent uptake of probes **1** and **2** at 20 μM by Hela cells (human cervical cells). (b) Fluorescence intensity quantitation was analyzed by the images.

Cellular uptake.

To demonstrate their biological applications, we performed fluorescence imaging in live HeLa cells by confocal laser scanning microscopy (CLSM). The time-dependent cellular uptakes of probes **1** and **2** were first evaluated in Hela cells at a concentration of

20 μM, respectively, as shown in Fig. 6a. Surprisingly, both probes showed efficient and ultrafast uptake in minutes. Especially, cellular fluorescence intensity of **1** reached a plateau in less than 10 min. It was observed that the cellular plasma can be clearly visualized with excellent image contrast to the cell background regardless of the washing or non-washing process after cell staining. Bright fluorescence and appearing cellular profiles (20 μM, incubated for 10 min, without PBS wash) were observed when the cells are incubated in plates (Figs. S23a and S23e).

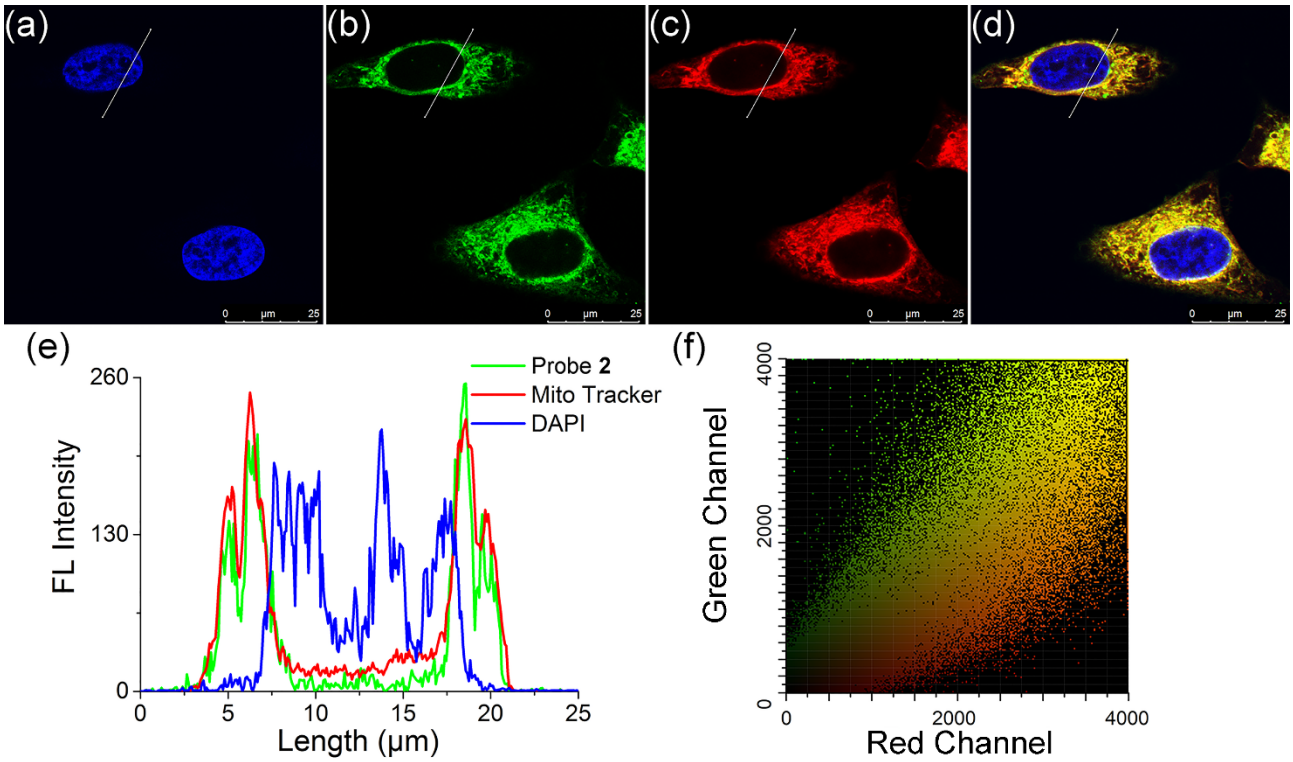

Fig. 7. Mitochondria-targeting properties of probe **2** (20 μM) in Hela cells. (a) 4',6-diamidino-2-phenylindole (DAPI, 0.08 μg/mL) fluorescence; (b) Probe **2** fluorescence after incubation for 0.5 h, using excitation wavelengths of 488 nm, and recording over the 500-800 nm spectral regions; (c) MitoTracker® Deep Red FM (0.5 μM) fluorescence, using excitation wavelengths of 635 nm, and recording over 650-800 nm spectral regions; (d) merged images of parts a, b and c; (e) intensity profiles within the regions of interests (ROIs) of Probe **2** and MitoTracker® Deep Red FM across Hela cells; (f) correlation plot of MitoTracker® Deep Red FM and probe **2** intensities. Scale bars = 25 μm. Pearson's correlation Rr = 0.92; Overlap coefficient R = 0.94.

Subcellular localization.

To further investigate the subcellular distributions of these two AIEgens in live cells, the colocalization experiments were performed using a commercially available mitochondria tracker, MitoTracker® Deep Red FM (MTDR). MTDR (0.5 μM) was co-stained with probe **1** or **2** (20 μM) in Hela cells, respectively. The cells were then incubated for 0.5 h. After fixed by 4% formaldehyde, the organelle tracer DAPI (0.08 μg/mL) was added subsequently and further incubated to stain the nucleus (Fig. 7a). Probe **2** marked with green pseudo color fluorescence (λ_{ex} at 488 nm, Fig. 7b) in Hela cells under a CLSM, while MTDR marked with red pseudo color (λ_{ex} at 635 nm Fig. 7c). The yellow area in the merged photo (Fig. 7d) showed the nice overlap of emission from probe **2** and MTDR. The fluorescence intensity profiles of the randomly selected regions across the Hela cells were calculated and showed a high Pearson's coefficient of 0.95 (Fig. 7e). Furthermore, the correlation plot of green (MTDR) channel and red (probe **2**) channel also gave a high Pearson's correlation coefficient (0.92) and a high overlap coefficient (0.94) (Fig. 7f), confirming that the probe

selectively targeted mitochondria in live cells. Similar to probe **2**, probe **1** also exhibited superior selectively toward mitochondria (Fig. S24).

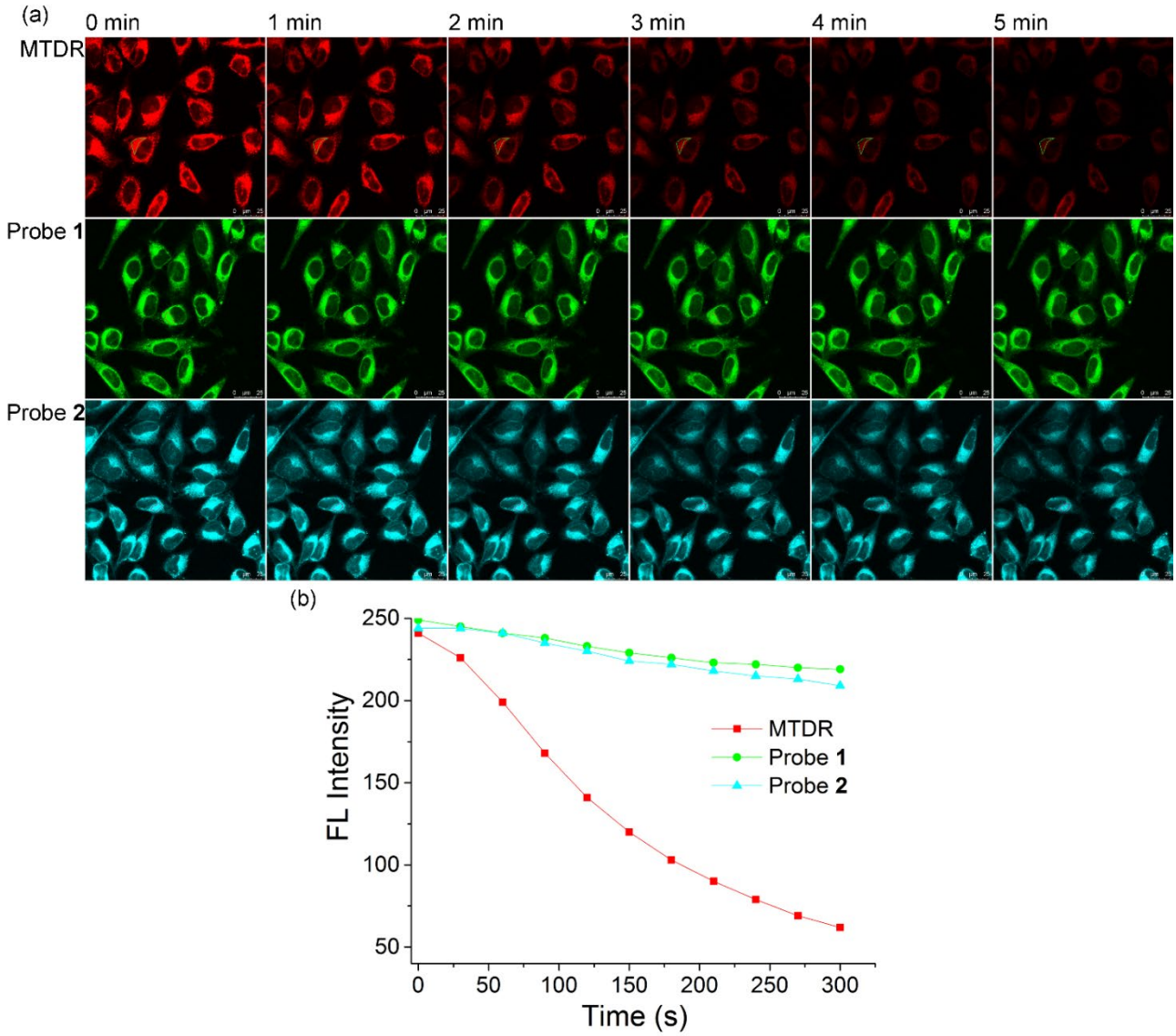

Fig. 8. (a) Fluorescent images and (b) fluorescence intensity of MDTR (λ_{ex} at 635 nm), probes **1** and **2** (λ_{ex} at 488 nm) by continuous irradiation at different time under the same laser intensity. The image was scanned about every 60 s. Scale bar: 25 μm.

Photostability.

Photostability is another crucial parameter for fluorescence imaging reagents. The photostability of probes **1** and **2** were first evaluated by continuous irradiation with confocal lasers. The fluorescence intensities of cells were detected and a time-dependent photostability diagram was developed with fluorescence intensities of cells as a vertical coordinate, and irradiation time as a horizontal coordinate (Fig. 8b). After 300 seconds light exposure, the fluorescence intensities of MTDR decreased approximately 75%. Under the same condition, the fluorescence intensities of both probes **1** and **2** decreased only by 12% and 13%, respectively. As seen in Fig 8a, the fluorescence signals of MTDR obviously decreased under the same voltage condition, while the fluorescence intensities of probes **1** and **2** showed negligible decrease after being irradiated 5 min by strong laser power.

Ex vivo tissue imaging

Inspired by the ultrafast penetrability and wash-free imaging in live cells for these BODIPY AIEgens, we further studied their ex vivo fluorescent imaging in domestic cat skeletal muscle tissues, respectively. After the incubation in tissues for 5 min, their fluorescent images for **1** and **2** were captured as shown in Figs. 9b and 9f, respectively. From these magnified fluorescent images (Figs. 9c and 9h), the texture of muscle tissue is clear and striated under excitation wavelengths of 488 nm, exhibiting a high signal-to-noise ratio. In addition, we observed their fluorescent images at a depth of 20 and 30 μm, respectively for **1** and **2** along the direction of z-axis, and successfully obtained their 3D fluorescent images (Figs. 9e and 9j). Such observations of these tissue staining patterns are in good agreement with previously reported results in rat skeletal muscle tissues.[31b]

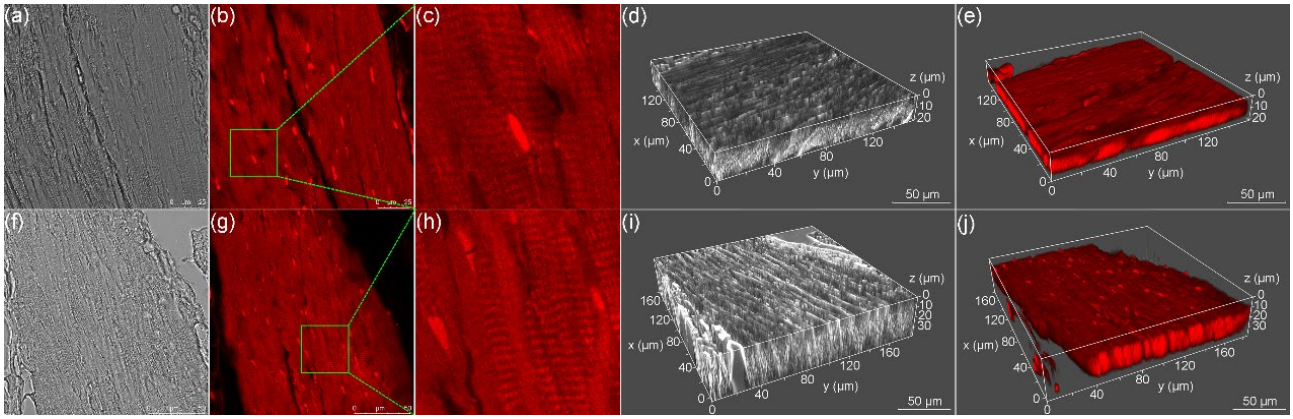

Fig. 9. Ex vivo fluorescent imaging in deep tissues. (a), (f) bright fields images of the domestic cat skeletal muscle tissue stained with probes **1** or **2** (20 μM); (b), (g) Fluorescence images of deep tissues with probes **1** and **2** after incubation for 5 min using excitation wavelengths of 488 nm, respectively; (c), (h) Fluorescent images magnification of selected deep tissues; (d), (i) reconstructed 3D bright fields images; (e), (j) reconstructed 3D fluorescent microscopic images.

CONCLUSION

In conclusion, we have successfully developed two novel *meso*-2-ketopyrrolyl BODIPY AIEgens *via* convenient condensation between 2-methylpyrrole and the corresponding pyrrolyldiketone in the presence of $BF_3 \cdot OEt_2$. While the two AIEgens showed very weak fluorescence in polar solvents due to the free rotation of *meso*-2-ketopyrrolyl group, both AIEgens gave intense and red-shifted fluorescence in aggregation state in water and in solid state. Both AIEgens could specifically stain and "light up" the cell mitochondria with high biocompatibility and an ultrafast and easy-to-operate staining protocol. Their fluorescent images in deep tissue penetration were captured with a relatively satisfied signal-to-noise ratio at a depth of 20 and 30 μm along the direction of z-axis. More importantly, both AIEgens exhibit high photostability under harsh continuous laser irradiation, demonstrating their potential application in visualizing and tracking specific mitochondria-associated dynamic changes.

EXPERIMENTAL

Materials and methods.

Reagents and solvents were used as received from commercial suppliers unless noted otherwise. Organelle tracers 4',6-diamidino-2-phenylindole (DAPI) and MitoTracker Deep Red FM (MTDR) were purchased from commercial supplier and used directly. All

reactions were performed in oven-dried or flame-dried glassware unless otherwise stated and were monitored by TLC using 0.25 mm silica gel plates with UV indicator. ^{1}H and ^{13}C NMR were recorded on 300 and 500 MHz NMR spectrometer at room temperature. Chemical shifts (δ) are given in ppm relative to internal TMS in $CDCl_3$ (7.26 ppm for ^{1}H and 77 ppm for ^{13}C). High-resolution mass spectra (HRMS) were obtained using APCI in positive mode. Scanning electron microscopic (SEM) images were obtained using a Hitachi SU-8010 instrument. Dynamic light scattering (DLS) investigations were carried out with an ALV/CGS-8F dynamic light.

Crystals suitable for X-ray crystallographic analysis.

Crystal of **2** (CCDC 1541730) suitable for X-ray analysis was obtained from the slow diffusion of hexane into its concentrated dichloromethane solution. Diffraction data were collected on a Bruker APEXII CCD area detector diffractometer using graphite-monochromated Mo-Kα radiation (λ = 0.71073 Å). An empirical absorption correction was applied with the SADABS program. Using Olex2, the structure was solved with the ShelXT structure solution program using direct methods and refined with the ShelXL refinement package using least squares minimisation.[32-34] The hydrogen atom coordinates were calculated with SHELXL by using an appropriate riding model with varied thermal parameters. The residual electron densities were of no chemical significance. These data can be obtained from the cambridge crystallographic data centre via www.ccdc.cam.ac.uk/data_request/cif.

Photophysical characterization

UV-visible absorption and fluorescence emission spectra were recorded on commercial spectrophotometers (200-900 nm scan range, Shimadzu UV-2450 and FS5) at room temperature (1 cm quartz *cuvette)*. Absolute fluorescence quantum efficiencies of the *meso*-2-ketopyrrolyl derived BODIPYs were obtained on Edinburgh FLS 1000 fluorescence spectrometer in organic solvents (excited at 480 nm) and solid states (excited at 550 nm). The yields were calculated by comparing the areas under the corrected emission of the sample in integrating sphere,[35] using eq 1 given below:

$$\Phi_F = \frac{N_{em}}{N_{abs}} = \frac{\alpha \int \frac{\lambda}{hc} I_{em}(\lambda) d\lambda}{\alpha \int \frac{\lambda}{hc} [I_{ex}(\lambda) - I'_{ex}(\lambda)] d\lambda} \qquad (1)$$

where N_{em} and N_{abs} are the numbers of emitted and absorbed photons, respectively, α is the calibration factor for the measurement setup, λ is the wavelength, h is the Plank's constant, c is the speed of light, $I_{em}(\lambda)$ is the emission intensity at λ, and $I_{ex}(\lambda)$ and $I'_{ex}(\lambda)$ are the intensities of the excitation laser beam with λ in the absence and presence of the sample, respectively. The measured Φ_F value is independent of sharp and thickness of sample and power of excitation laser.

Synthesis of BODIPY 1.

Pyrrolyldiketone **3a** (195 mg, 0.8 mmol) was dissolved in distilled dichloromethane (60 mL). After adding 0.2 mL $BF_3{\cdot}OEt_2$, the mixture turned brown quickly. A solution of 2-methylpyrrole (0.2 mL) in distilled dichloromethane (2 mL) was dropwise added. The reaction mixture was stirred at room temperature (35 °C) and monitored with TLC. After dipyrrolyldiketone **3a** was exhausted, 2 mL of Et_3N was added into the mixture. The reaction mixture was stirred for 3 h before the subsequent addition of $BF_3{\cdot}OEt_2$ (3 mL) through syringe. After the mixture was further stirred for 1 h, it was poured into water and extracted with dichloromethane (30 mL × 3). Then, the organic phase was combined, washed with saturated $NaHCO_3$ solution, dried over anhydrous Na_2SO_4, filtered and rotary evaporated. The crude product was purified by column chromatography on silica gel (hexane/EtOAc = 4/1, v/v) and was further recrystallized from hexane to give probe **1** as reddish powders in 28% yield (80 mg). ^{1}H NMR (300 MHz, $CDCl_3$) δ 9.59 (s, 1H), 6.72 (d, *J* = 3.8 Hz, 1H), 6.19 (d, *J* = 3.9 Hz, 1H), 6.07 (s, 1H), 5.85 (s, 1H), 2.59 (s, 6H), 2.31 (s, 3H), 1.96 (s, 3H), 1.89 (s, 3H). ^{13}C NMR (126 MHz, $CDCl_3$) δ 177.9, 160.1, 156.4, 143.3, 139.2, 138.1, 134.1, 131.8, 130.1, 128.7, 127.2, 121.8, 118.9, 114.1, 15.2, 15.0, 13.7, 13.5, 13.2. HRMS (APCI) calcd. for $C_{19}H_{21}BF_2N_3O$ $[M + H]^+$: 356.1740, found 356.1740.

Synthesis of BODIPY 2.

Probe **2** was prepared using the above procedure from pyrrolyldiketone **3b** (240 mg, 0.8 mmol) and 2-methylpyrrole (0.2 mL) affording a reddish powder in 23% yield (75 mg). ^{1}H NMR (300 MHz, $CDCl_3$) δ 9.47 (s, 1H), 6.65 (d, *J* = 3.4 Hz, 1H), 6.14 (d, *J* = 3.4 Hz, 1H), 2.58 (s, 6H), 2.43 - 2.23 (m, 7H), 1.89 (s, 3H), 1.84 (s, 3H), 1.04 (m, 6H). ^{13}C NMR (126 MHz, $CDCl_3$) δ 177.9, 160.2, 154.6, 139.1, 137.5, 136.6, 134.6, 131.5, 131.2, 130.0, 128.0, 126.3, 126.1, 117.8, 17.3, 15.2, 14.9, 14.6, 13.3, 12.0, 11.3, 10.8.

HRMS (APCI) calcd. for $C_{23}H_{29}BF_2N_3O$ $[M + H]^+$: 412.2366, found 412.2364.

Preparation of solutions

BODIPYs **1** or **2** in DMSO solution (10 mM) were used as mother solution. A certain amount of corresponding volumes of the mother solution were injected into deionized water or 1640 complete medium under sonication, respectively. The sudden solubility decreases in poor solvents resulted in self-assembly of the π-conjugated probe **1** or **2** into corresponding NPs.[6c]

Cell incubation and colocalization imaging.

A total of 30000 HeLa cells were seeded into a glass bottom dish and were cultured in culture media (RPMI-1640, supplemented with 10% FBS) at 37 °C in an atmosphere of 5% CO_2 and 95% humidified atmosphere for 24 h. HeLa cells were first stained with probes **1** or **2** (20 μM, 1% DMSO and 99% 1640 complete medium) at 37 °C in an atmosphere of 5% CO_2 for 0.5 h. After washing the plates two times with PBS, the cells were fixed by 4% formaldehyde for 20 min. The organelle tracer 4',6-diamidino-2-phenylindole (DAPI, 0.08 μg/mL) was added subsequently and was incubated for 30 min to stain the nucleus. Finally, the plates were washed again with PBS and the morphologies of the HeLa cells were observed using a confocal fluorescence microscope (Leica Microsystems SP8 MP, excitation at 405, 488 and 638 nm for DAPI, probes **1** or **2**, and MitoTracker® Deep Red FM, respectively).

Cellular uptake.

A total of 30000 HeLa cells were seeded into a glass bottom dish and were cultivated in RPMI-1640 with 10% FBS at 37°C, 5% CO_2 and 95% humidity for 24 h. Probes **1** or **2** (20 μM, 1% DMSO and 99% 1640 complete medium) were cultivated with HeLa cells for 1, 5, 10, 30, 60 and 120 min, respectively. The above cells were washed twice with PBS. Then these cells were used to measure the fluorescence intensity using a confocal fluorescence microscope.

Cytotoxicity determined by the CCK-8 method.

The HeLa cells (5000) per well were seeded on 96-well plates and incubated in 1640 complete medium for 24 h at 37 °C. Then, a gradient concentration of probes **1** or **2** from 0.1 to 200 μM in a fresh medium were added into the 96-well plate, and the cells with the probe were incubated at 37 °C. Each experiment was performed for at least three times. After 24 h, the working solutions were then removed, and the cells were washed with PBS buffer for two times. A total of 10 μL of CCK-8 (Cell Counting Kit-8, BIOMIKY) was added into each well, and the cells were further incubated at 37 °C for 1.5 h. Then the plate was shaken for 5 min, and the absorbance at 450 nm was measured with a microplate reader (Multiskan Sky).

Ex vivo imaging in cat skeletal muscle tissues.

The domestic cat skeletal muscle tissues were bought from Fenghua teaching company limited. The tissues were stained with probes **1** or **2** (20 μM) at room temperature in culture medium (RPMI-1640, supplemented with 10% FBS and 1% penicillin and streptomycin) in 5% CO_2/air at 37 °C in a humidified incubator for 5 min. The tissues were then directly used for imaging under excitation wavelengths of 488 nm.

Photostability.

A total of 30000 HeLa cells were seeded into a glass bottom dish and were cultured in culture media (RPMI-1640, supplemented with 10% FBS) at 37 °C in an atmosphere of 5% CO_2 and 95% humidified atmosphere for 24 h. The cells with the probes **1** or **2** were incubated at 37 °C for 10 min and MTDR were incubated at 37 °C for 30 min in another dish. For photostability test, cells were continuously irradiated with confocal lasers under the same laser power. The image was captured about every 60 s.

ACKNOWLEDGEMENT.

We thank the financial supports from the the National Natural Science Foundation of China (Grants Nos. 21672006, 21672007, 21871006, 21971004 and 21402001), Open Fund of Nanjing University State Key Laboratory of Coordination Chemistry (SKLCC1911), Hong Kong Research Grants Council (C6009-17G) and Hong Kong Polytechnic University (1-YW2T).

REFERENCES:

[1] a) Ow YLP, Green DR, Hao Z, Mak TW. Cytochrome c: functions beyond respiration. Nat Rev Mol Cell Biol 2008;9:532-42. b) Levine B, Kroemer G. Autophagy in the pathogenesis of disease. Cell 2008;132:27-42.

[2] Hoye AT, Davoren JE, Wipf P, Fink MP, Kagan VE. Targeting mitochondria. Acc Chem Res 2008;41:87-97.

[3] a) Marian AJ, Bhatnagar A, Bolli R, Belmonte JCI. Introduction to cardiovascular aging compendium. Circ Res 2018;123:737-39. b) Laker RC, Xu P, Ryall KA, Sujkowski A, Kenwood BM, Chain KH, et al. A novel mito timer reporter gene for mitochondrial content, structure, stress, and damage in vivo. J Bio Chem 2014;289:12005-15.

[4] Zheng Z, Zhang T, Liu H, Chen Y, Kwok RTK, Ma C, et al. Bright near-infrared aggregation-induced emission luminogens with strong two-photon absorption, excellent organelle specificity and efficient photodynamic therapy. ACS Nano 2018;12:8145-59.

[5] Samkoe KS, Bates BD, Elliott JT, LaRochelle E, Gunn JR, Marra K, et al. Application of fluorescence-guided surgery to subsurface cancers requiring wide local excision: literature review and novel developments toward indirect visualization. Cancer Control 2018;25:1073274817752332.

[6] a) Leung CWT, Hong Y, Chen S, Zhao E, Lam JWY, Tang BZ. A photostable AIE luminogen for specific mitochondrial imaging and tracking. J Am Chem Soc 2013;135:62-5. b) Che W, Zhang L, Li Y, Zhu D, Xie Z, Li G, et al. Ultrafast and noninvasive long-term bioimaging with highly stable red aggregation-induced emission nanoparticles. Anal Chem 2019;91:3467-74. c) Niu G, Zhang R, Gu Y, Wang J, Lam JWY, Sung HHY, et al. Highly photostable two-photon NIR AIEgens with tunable organelle specificity and deep tissue penetration. Biomaterials 2019;208:72-82.

[7] a) Förster T, Kasper K. Ein konzentrationsumschlag der fluoreszenz. Z Phys Chem 1954; 1: 275-7. b) Ding D, Li K, Liu B, Tang BZ. Bioprobes based on AIE fluorogens. Acc Chem Res 2013;46:2441-53.

[8] a) Luo M, Wang S, Li C, Miao W, Ma X. Aggregation-induced emission organogel formed by both sonication and thermal processing based on tetraphenylethylene and cholesterol derivative. Dyes Pigments 2019;165:436-43. b) Huang Y, Mei J, Ma X. A novel simple red emitter characterized with AIE plus intramolecular charge transfer effects and its application for thiol-containing amino acids detection. Dyes Pigments 2019;165:499-507.

[9] Luo J, Xie Z, Lam JWY, Cheng L, Chen H, Qiu C, et al. Aggregation-induced emission of 1-methyl-1,2,3,4,5-pentaphenylsilole. Chem Commun 2001;18:1740-1.

[10] Mei J, Hong Y, Lam JWY, Qin A, Tang Y, Tang BZ. Aggregation-induced emission: the whole is more brilliant than the parts. Adv Mater 2014;26:5429-79.

[11] Mei J, Leung NLC, Kwok RTK, Lam JWY, Tang BZ. Aggregation-induced emission: together we shine, united we soar. Chem Rev 2015;115:11718-940.

[12] a) Wang D, Su H, Kwok RTK, Hu X, Zou H, Luo Q, et al. Rational design of a water-soluble NIR AIEgen, and its application in ultrafast wash-free cellular imaging and photodynamic cancer cell ablation. Chem Sci 2018;9:3685-93. b) Chen M, Hu X, Liu J, Li B, Leung NLC, Viglianti L, et al. Rational design of red AIEgens with a new core structure from non-emissive heteroaromatics. Chem Sci 2018;9:7829-34.

[13] Kokado K, Sada K. Consideration of molecular structure in the excited state to design new luminogens with aggregation-induced emission. Angew Chem Int Ed 2019;58:8632-9.

[14] Liu Z, Jiang Z, Yan M, Wang X. Recent progress of BODIPY dyes with aggregation-induced emission. Front Chem 2019;7:712.

[15] a) Zhang W, Kwok RTK, Chen Y, Chen S, Zhao E, Yu C, et al. Real-time monitoring of the mitophagy process by a photostable fluorescent mitochondrion-specific bioprobe with AIE characteristics. Chem Commun 2015;51:9022-5. b) Situ B, Chen S, Zhao E, Leung CWT, Chen Y, Hong Y, et al. Real-time imaging of cell behaviors in living organisms by a mitochondria-targeting AIE fluorogen. Adv Funct Mater 2016;26:7132-8. c) Nicol A, Qin W, Kwok RTK, Burkhartsmeyer JM, Zhu Z, Su H, et al. Functionalized AIE nanoparticles with efficient deep-red emission, mitochondrial specificity, cancer cell selectivity and multiphoton susceptibility. Chem Sci 2017;8:4634-43. d) Liu L, Zou Q, Leung JK, Wang JL, Kam C, Chen S, et al. Ultrafast labeling and high-fidelity imaging of mitochondria in cancer cells with an aggregation-enhanced emission fluorescent probe. Chem Commun 2019;55:14681-4.

[16] Shin WP, Lee MG, Verwilst P, Lee JH, Chi SG, Kim JS. Mitochondria-targeted aggregation induced emission theranostics:

crucial importance of in situ activation. Chem Sci 2016;7:6050-9.
[17] a) Yao Q, Li L, Huang X, Li H, Fang Y, Xia J, et al. Photostable fluorescent tracker for imaging mitochondria with super resolution. Anal Chem 2019;91:15777-83. b) Li J, Kwon N, Jeong Y, Lee S, Kim G, Yoon J. Aggregation-induced fluorescence probe for monitoring membrane potential changes in mitochondria. ACS Appl Mater Inter 2018;10:12150-4.
[18] a) Zhang B, Feng G, Wang S, Zhang X. Boronic acid derived salicylidenehydrazone complexes for wash-free fluorescence imaging of cellular organelles. Dyes Pigments 2018;149:356-62. b) Zou J, Lu H, Zhao X, Li W, Guan Y, Zheng Y, Zhang L, Gao H. A multi-functional fluorescent probe with aggregation-induced emission characteristics: mitochondrial imaging, photodynamic therapy and visualizing therapeutic process in zebra fish model. Dyes Pigments 2018;151:45-53. c) Zhu L, Fu M, Yin B, Wang L, Chen Y, Zhu Q. A red-emitting fluorescent probe for mitochondria-target microviscosity in living cells and blood viscosity detection in hyperglycemia mice. Dyes Pigments 2020;172:107859.
[19] a) Boens N, Leen V, Dehaen W. Fluorescent indicators based on BODIPY. Chem Soc Rev 2012;41:1130-72. b) Lu H, Mack J, Yang Y, Shen Z. Structural modification strategies for the rational design of red/NIR region BODIPYs. Chem Soc Rev 2014;43:4778-823. c) Boens N, Verbelen B, Dehaen W. Postfunctionalization of the BODIPY Core: synthesis and spectroscopy. Eur J Org Chem 2015;30:6577-95. d) Orte A, Debroye E, Ruedas-Rama MJ, Garcia-Fernandez E, Robinson D, Crovetto L, et al. Effect of the substitution position (2, 3 or 8) on the spectroscopic and photophysical properties of BODIPY dyes with a phenyl, styryl or phenylethynyl group. RSC Adv 2016;6:102899-913. e) Chong H, Fron E, Liu Z, Boodts S, Thomas J, Harvey JN, et al. Acid-sensitive BODIPY dyes: synthesis through Pd-catalyzed direct C(sp3)-H arylation and photophysics. Chem Eur J 2017;23:4687-99. f) Leen V, Laine M, Ngongo JM, Lipkowski P, Verbelen B, Kochel A, et al. Impact of the keto-enol tautomeric equilibrium on the BODIPY chromophore. J Phys Chem A 2018;122:5955-61. g) Kolemen S, Akkaya EU. Reaction-based BODIPY probes for selective bio-imaging. Coord Chem Rev 2018;354:121-34.
[20] a) Zhao N, Williams TM, Zhou Z, Fronczek FR, Sibrian-Vazquez M, Jois SD, et al. Synthesis of BODIPY-peptide conjugates for fluorescence labeling of EGFR overexpressing cells. Bioconjugate Chem 2017;28:1566-79. b) LaMaster DJ, Kaufman NEM, Bruner AS, Vicente MGH. Structure based modulation of electron dynamics in meso-(4-pyridyl)-BODIPYs: a computational and synthetic approach. J Phys Chem A 2018;122:6372-80. c) Zhang G, Zhao N, Bobadova-Parvanova P, Wang M, Fronczek FR, Smith KM, et al. Syntheses, spectroscopic properties, and computational study of (E,Z)-ethenyl and ethynyl-linked BODIPYs. J Phys Chem A 2018;122:6256-65. d) Wang M, Zhang G, Bobadova-Parvanova P, Merriweather AN, Odom L, Barbosa D, et al. Syntheis and investigation of linker-free BODIPY-Gly conjugations substituted at the boron atom. Inorg Chem 2019;58:11614-21.
[21] a) Yu Y, Jiao L, Wang J, Wang H, Yu C, Hao E et al. Bu_4NI/tBuOOH catalyzed, α-regioselective cross-dehydrogenative coupling of BODIPY with allylic alkenes and ethers. Chem Commun 2017;53:581-584. b) Lv F, Yu Y, Hao E, Yu C, Wang H, Jiao L, et al. Copper-catalyzed α-benzylation of BODIPYs via radical-triggered oxidative cross-coupling of two C-H bonds. Chem Commun 2018;54:9059-62. c) Wang D, Cheng C, Wu Q, Wang J, Kang Z, Guo X, Wu H, Hao E, Jiao L. Visible-light excitation of BODIPYs enables self-promoted radical arylation at their 3,5-positions with diazonium salts. Org Lett 2019;21:5121-5. d) Sheng W, Lv F, Tang B, Hao E, Jiao L. Toward the most versatile fluorophore: Direct functionalization of BODIPY dyes via regioselective C–H bond activation. Chin Chem Lett 2019;30:1825-33. e) Lv F, Tang B, Hao E, Liu Q, Wang H, Jiao L. Transition-metal-free regioselective cross-coupling of BODIPYs with thiols. Chem Commun 2019; 55:1639-42. f) Tang B, Lv F, Chen K K, Jiao L, Liu Q, Wang H, Hao E. Development of BODIPY dyes with versatile functional groups at 3,5-positions from diacyl peroxides via Cu(II)-catalyzed radical Alkylation. Chem Commun 2019;55:4691-4.
[22] a) Ma F, Zhou L, Liu Q, Li C, Xie Y. Selective photocatalysis approach for introducing ArS units into BODIPYs through thiyl radicals. Org. Lett. 2019;21:733-6. b) Teng KX, Niu LY, Li J, Jia L, Yang QZ. An unexpected coupling-reduction tandem reaction for the synthesis of alkenyl-substituted BODIPYs. Chem Commun 2019;55:13761-4. c) Duan C, Zhou Y, Shan GG, Chen Y, Zhao W, Yuan D, et al. Bright solid-state red-emissive BODIPYs: facile synthesis and their high-contrast mechanochromic properties. J Mater Chem C 2019;7:3471-8. d) Hu R, Lager E, Aguilar-Aguilar A, Liu J, Lam JWY, Sung HHY, Williams ID, Zhong Y, Wong KS, Penã-Cabrera E, Tang BZ. Twisted intramolecular charge transfer and aggregation-induced emission of BODIPY derivatives. J Phys Chem C 2009;113:15845-53.
[23] a) Wang S, Liu H, Mack J, Tian J, Zou B, Lu H, et al. A bodipy-based 'turn-on' fluorescent probe for hypoxic cell imaging. Chem Commun 2015;51:13389-92. b) Lu H, Mack J, Nyokong T, Kobayashi N, Shen Z. Optically active bodipys. Coord Chem Rev 2016;318:1-15. c) Wu Y, Wang S, Li Z, Shen Z, Lu H. Chiral binaphthyl-linked BODIPY analogues: synthesis and spectroscopic properties. J Mater Chem C 2016;4:4668-74. d) Zheng X, Du W, Gai L, Xiao X, Li Z, Xu L, et al. Disilanylene-bridged BODIPY-based D-σ-A architectures: a novel promising series of NLO chromophores. Chem Commun 2018;54:8834-7. e) Sun Y, Yuan H, Di

L, Zhou Z, Gai L, Xiao X. Non-symmetric thieno[3,2-b]thiophene-fused BODIPYs: synthesis, spectroscopic properties and providing a functional strategy for NIR probes. Org Chem Front 2019;6:3961-8. f) Kong X, Di L, Fan Y, Zhou Z, Feng X, Gai L, et al. Lysosome-targeting turn-on red/NIR BODIPY probes for imaging hypoxic cells. Chem Commun 2019;55:11567-70.

[24] a) Zhang X, Xiao Y, Qi J, Qu J, Kim B, Yue X, et al. Long-wavelength, photostable, two-photon excitable BODIPY fluorophores readily modifiable for molecular probes. J Org Chem 2013;78:9153-60. b) Wang F, Zhu Y, Zhou L, Pan L, Cui Z, Fei Q, et al. Fluorescent in situ targeting probes for rapid imaging of ovarian-cancer-specific γ-glutamyltranspeptidase. Angew Chem Int Ed 2015;54:7349-53. c) Kim JY, Sahu S, Yau YH, Wang X, Shochat SG, Nielsen PH, et al. Detection of pathogenic biofilms with bacterial amyloid targeting fluorescent probe, CDy11. J Am Chem Soc 2016;138:402-7.

[25] a) Choi S, Bouffard J, Kim Y. Aggregation-induced emission enhancement of a meso-trifluoromethyl bodipy via J-aggregation. Chem Sci 2014;5:751-5. b) Chua H, Ni Y, Garai M, Zheng B, Huang KW, Xu QH, et al. Towards meso-ester bodipys with aggregation-induced emission properties: the effect of substitution positions. Chem Asian J 2015;10:1631-4. c) Kim S, Bouffard J, Kim Y. Tailoring the solid-state fluorescence emission of bodipy dyes by meso substitution. Chem Eur J 2015;21:17459-65.

[26] a) Hu R, Gómez-Durán CFA, Lam JWY, Belmonte-Vázquez JL, Deng C, Chen S, et al. Synthesis, solvatochromism, aggregation-induced emission and cell imaging of tetraphenylethene-containing BODIPY derivatives with large Stokes shifts. Chem Commun 2012;48:10099-100. b) Feng HT, Xiong JB, Zheng YS, Pan B, Zhang C, Wang L, et al. Multicolor emissions by the eynergism of intra/intermolecular slipped π-π stackings of tetraphenylethylene-diBODIPY conjugate. Chem Mater 2015;27:7812-9. c) Gómez-Durán CFA, Hu R, Feng G, Li T, Bu F, Arseneault M, et al. Effect of AIE substituents on the fluorescence of tetraphenylethene-containing BODIPY derivatives. ACS Appl Mater Interfaces 2015;7:15168-76. d) Feng HT, Gu X, Lam JWY, Zheng YS, Tang BZ. Design of multi-functional AIEgens: tunable emission, circularly polarized luminescence and self-assembly by dark through-bond energy transfer. J Mater Chem C 2018;6:8934-40. e) Zhou J, Xu S, Yu Z, Ye X, Dong X, Zhao W. Two-channel responsive fluorescent probe of meso carboxylate of BODIPY with AIE characteristics for fast detection of palladium. Dyes Pigments 2019;170:107656.

27) a) Kuimova MK, Yahioglu G, Levitt JA, Suhling K. Molecular rotor measures viscosity of live cells via fluorescence lifetime imaging. J Am Chem Soc 2008;130:6672-3. b) Yang Z, He Y, Lee JH, Park N, Suh M, Chae WS, et al. A self-calibrating bipartite viscosity sensor for mitochondria. J Am Chem Soc 2013;135:9181-5. c) Wang L, Xiao Y, Tian W, Deng L, Activatable rotor for quantifying lysosomal viscosity in living cells. J Am Chem Soc 2013;135:2903-6. d) Zhu H, Fan J, Li M, Cao J, Wang J, Peng X. A "distorted-BODIPY"-based fluorescent probe for imaging of cellular viscosity in live cells. Chem Eur J 2014;20:4691-6. e) Li LL, Li K, Li MY, Shi L, Liu YH, Zhang H, et al. BODIPY-based two-photon fluorescent probe for real-time monitoring of lysosomal viscosity with fluorescence lifetime imaging microscopy. Anal Chem 2018; 90:5873-8. f) He Y, Shin J, Gong W, Das P, Qu J, Yang Z, et al. Dual-functional fluorescent molecular rotor for endoplasmic reticulum microviscosity imaging during reticulophagy. Chem Commun 2019;55:2453-6.

28) a) Kee HL, Kirmaier C, Yu L, Thamyongkit P, Youngblood WJ, Calder ME, et al. Structural control of the photodynamics of boron-dipyrrin complexes. J Phys Chem B 2005;09:20433-43. b) Bahaidarah E, Harriman A, Stachelek P, Rihn S, Heyer E, Ziessel R. Fluorescent molecular rotors based on the BODIPY motif: effect of remote substituents. Photochem Photobiol Sci 2014;13:1397-401.

29) Levitt JA, Kuimova MK, Yahioglu G, Chung PH, Suhling K, Phillips D. Membrane-bound molecular rotors measure viscosity in live cells via fluorescence lifetime imaging. J Phys Chem C 2009;113:11634-42.

[30] a) Yu C, Huang Z, Gu W, Wu Q, Hao E, Xiao Y, et al. A novel family of AIE-active meso-2-ketopyrrolyl BODIPYs: bright solid-state red fluorescence, morphological properties and application as viscosimeters in live cells. Mater Chem Front 2019;3:1823-32. b) Miao W, Yu C, Hao E, Jiao L. Functionalized BODIPYs as fluorescent molecular rotors for viscosity detection. Front Chem 2019;7:825.

[31] a) Zhang X, Zhang X, Tao L, Chi Z, Xu J, Wei Y. Aggregation induced emission-based fluorescent nanoparticles: fabrication methodologies and biomedical applications. J Mater Chem B 2014;2:4398-414. b) Zhang R, Sun Y, Tian M, Zhang G, Feng R, Li X, et al. A phospholipid-biomimetic fluorescent mitochondrial probe with ultrahigh selectivity enables in-situ and high-fidelity tissue imaging. Anal Chem 2017;89:6575-82 .

[32] Dolomanov OV, Bourhis LJ, Gildea RJ, Howard JAK, Puschmann H. Olex2: a complete structure solution, refinement and analysis program. J Appl Cryst 2009;42:339-41.

[33] Sheldrick GM. SHELXT-integrated space-group and crystal-structure determination. Acta Cryst 2015;A71:3-8.

[34] Sheldrick GM. A short history of SHELX. Acta Cryst 2008;A64:112-22.

[35] Kawamura Y, Sasabe H, Adachi C. Simple accurate system for measuring absolute photoluminescence quantum efficiency in organic solid-state thin films. Jpn J Appl Phys 2004;43:7729-30.